energies

MDPI

Article

A Novel Wind Energy Gathering Structure for the Savonius Wind Turbine and Its Parameter Optimization Based on Taguchi's Method

Tianjiao Zhang [1,2] and Shuhui Xu [1,2,*]

[1] School of Mechanical Engineering, Qilu University of Technology (Shandong Academy of Sciences), Jinan 250353, China; 17353308635@163.com
[2] Shandong Institute of Mechanical Design and Research, Jinan 250353, China
* Correspondence: xushuhui@qlu.edu.cn

Abstract: An auxiliary structure can significantly improve the wind-trapping capacity of the Savonius wind turbine. In this study, a novel auxiliary structure called a wind energy gathering structure (WEGS) is proposed, and its five parameters, namely the lengths of the shrinkage and diffusion tubes, the length of the centerboard, the length of the throat, the length of the wind board, and the shrinkage and diffusion angles, are investigated using computational fluid dynamics (CFD) and Taguchi's method. Meanwhile, Taguchi's method and ANOVA reveal that among the studied parameters, the shrinkage and diffusion angles, the length of the centerboard, and the lengths of the shrinkage and diffusion tubes have a more significant influence on the performance of the WEGS. At a tip speed ratio (*TSR*) value of 1 and a wind speed of 7 m/s, the optimized combination of the WEGS parameters obtained by Taguchi's method improves the mean torque coefficient of the turbine by 42.1%. Moreover, at other *TSRs* (0.6–1.2), the turbine with the WEGS also outperforms an open turbine in terms of aerodynamic (increases of 20.1–53%) and lifetime performance.

Keywords: Savonius wind turbine; WEGS; CFD; Taguchi's method; ANOVA

check for updates

Citation: Zhang, T.; Xu, S. A Novel Wind Energy Gathering Structure for the Savonius Wind Turbine and Its Parameter Optimization Based on Taguchi's Method. *Energies* **2024**, *17*, 5348. https://doi.org/10.3390/en17215348

Academic Editor: Davide Astolfi

Received: 28 September 2024
Revised: 17 October 2024
Accepted: 23 October 2024
Published: 28 October 2024

Copyright: © 2024 by the authors. Licensee MDPI, Basel, Switzerland. This article is an open access article distributed under the terms and conditions of the Creative Commons Attribution (CC BY) license (https://creativecommons.org/licenses/by/4.0/).

1. Introduction

The increasing energy dependence of today's society and the depletion of non-renewable energy sources, along with the associated environmental issues, have captured the attention of humankind. Renewable energy includes wind, water, solar, biomass, and geothermal energy [1]. Wind energy has proven to be a reliable and environmentally friendly alternative to fossil fuels [2]. The role of wind turbines is to convert wind energy into electricity [3]. In the last decade or so, wind power technology has been developing at such a pace that the total installed capacity of wind turbines worldwide has risen from more than 300 GW in 2010 to 923 GW in 2022, and the Global Wind Energy Council predicts that the total installed capacity could reach 1210 GW by 2025 [4]. According to the difference in rotational axis steering, wind turbines can be classified into vertical axis wind turbines (VAWTs) and horizontal axis wind turbines (HAWTs) [5]. HAWTs have been extensively studied in recent decades due to their higher efficiency compared to VAWTs [6]. However, in recent years, VAWTs have gained considerable attention in a variety of applications due to their simple structure, compact construction, and high potential for use in small- and medium-sized power generation facilities. In addition, VAWTs offer advantages such as environmental friendliness and cost-effectiveness, making them well suited for residential, suburban, and commercial areas [7–9]. However, their limited ability to capture wind has prevented the Savonius wind turbines from being widely used in communities and residential areas to meet the electricity needs of the population.

The Savonius wind turbine is a type of VAWT that has attracted growing attention from researchers due to its uncomplicated conformation and high self-starting capability [10]. Nevertheless, its limited capacity for capturing wind has hindered its widespread

application and promotion. Consequently, numerous researchers have focused on optimizing this type of turbine by addressing three key aspects. Firstly, the fundamental parameters of the Savonius wind turbine were optimized. M.H. Nasefa et al. [11] investigated the simulation accuracy of different turbulence models adopted when using CFD to study the performance of this type of turbine and studied the effect of the overlap ratio on the performance of the turbine. According to their research results, the SST *k*-ω model can achieve superior simulation accuracy, and 0.15 is a good choice for the overlap ratio. U.K. Saha et al. [12] conducted experiments on three different numbers of blades for one-stage, two-stage, and three-stage rotors in a wind tunnel, showing that no matter how many stages of rotors there are, the best choice of blade is a double blade, and the two-stage rotor has a better power coefficient. Z. Zhao [13] found that the mean power coefficient of Savonius wind turbines increased with a larger AR in the range of $1 < AR < 6$. Thiyagaraj et al. [14] investigated the blade overlap ratio and the number of blades and proved that the best energy capture effect of the turbine was obtained when the number of blades was two and the overlap ratio was 0.2. Secondly, the blade shape was optimized. The wind-trapping capacity of the turbine can be improved by rationally changing the blade shape. Sonu Sharma et al. [15] designed a wind turbine with multiple quarter blades, which improved the maximum C_p by 8.89% compared to a conventional wind turbine. After designing a turbine with quarter blades, Sonu Sharma et al. [16] were inspired to propose a micro-blade to improve the performance of the wind turbine, which ultimately resulted in a performance improvement of 11.34% compared to an open turbine. Hassan A. Hassan Saeed et al. [17] predicted a new type of blade using a modified Adjoint Solver with an average torque coefficient of 23.9%. Islam Abdelghafar et al. [18], inspired by the sand eel, designed a bionic blade considering two key parameters, the maximum blade camber and the maximum blade camber position, and 128 combinations were evaluated by 2D numerical simulation. The optimal combinations resulted in a 9.21% increase in the average power coefficient at $TSR = 0.8$. M. Chan et al. [19] proposed a GA combined with CFD to optimize the blade, which improved the power coefficient by 33% compared to the traditional semicircular blade at $TSR = 0.8$, and improved the wind-trapping capacity of the blade in the range of $TSR = 0.6$–1.2. Mahmoud Ahmed et al. [20] proposed a twisted blade to improve the wind-trapping capacity of the Savonius wind turbine and ultimately found that the highest power coefficient was achieved when the twist angle was 45°and the overlap ratio was 0. Another alternative approach to improving the wind-trapping capacity of the turbine is to add auxiliary structures around the turbine blades. Some studies [21–24] have been conducted to enhance the wind-trapping capacity of wind turbines by placing deflectors, and the results have shown that the proper placement and shape of the deflectors can improve the mean power coefficient of the turbine by 8.78% to 30% and can effectively improve the self-starting ability of the turbine. Ali Hesami et al. [25] categorized the wind lens structure into six key parameters, and then studied them separately for single and double rotors, showing that the average power coefficients of the single and double rotors were improved by 64% and 114%, respectively, compared to the open turbine. Mohamed H. et al. [26] used OPAL coupled with CFD to optimize the positions of multiple guide plates, with a final performance improvement of 39.8%. Sammy Jamar Chemengich [27] designed an interstitial flow conduit to obtain a maximum performance improvement of 12.24% when the gap flow guide was 75°.

Based on the above research, the basic parameter optimization system is more mature, and it is difficult to make major breakthroughs. Although blade optimization is also a prominent methodology to improve the wind-trapping capacity of the Savonius wind turbine, its small improvement in the average power coefficient is also one of its shortcomings. In contrast, a proper auxiliary structure can significantly improve the wind-trapping capacity of Savonius wind turbines.

In this paper, a new auxiliary structure, named the wind energy gathering structure (WEGS), is proposed based on the working mechanism of the turbine. Meanwhile, the impacts of the five main parameters of the WEGS are investigated using Taguchi's method

and CFD simulation, and the optimal combinations of these parameters are obtained with the help of ANOVA analysis. Furthermore, the benefits of the WEGS on the energy capture ability and the service life of the turbine are analyzed. The key innovations of this work are as follows:

1. A new auxiliary structure, the WEGS, is proposed.
2. The effect of five parameters of the WEGS, i.e., the length of the shrinkage and diffusion tubes, the length of the centerboard, the length of the throat, the length of the wind board, and the shrinkage and diffusion angle, on the mean power coefficient of the turbine is investigated by Taguchi's method and ANOVA, and the optimal combination and key factors of them are obtained.
3. The reason why the WEGS can improve the wind-trapping capacity and the service life of the turbine is analyzed.

The rest of this article is organized as follows: Section 2 mainly gives an introduction to the structural parameters of the turbine, the theoretical foundations, and the parameterization of the WEGS. Section 3 details the construction of the CFD simulation environment to lay the foundation for the subsequent studies. Section 4 focuses on the optimization process and methodology of this work. Section 5 verifies the optimization results with CFD and analyzes the principle of using the WEGS to enhance the wind-trapping capacity. Section 6 sums up the research results obtained in this paper and indicates the direction for future research.

2. Savonius Wind Turbines and WEGS Structures

2.1. Geometry and Parameters

The Savonius wind turbine works on the principle that as the wind transits the turbine, it can create different pressures on the two blades, forming a torque that causes the blade to rotate [28]. A three-dimensional plot of the turbine, where H indicates the turbine height, is shown in Figure 1a. Figure 1b shows a two-dimensional schematic of the turbine consisting of an advancing blade and a returning blade, where d indicates the diameter of the single blade, D refers to the turbine diameter, S indicates the overlap length between the two blades, D_R refers to the diameter of the end plate, and e indicates the overlap ratio (S/d). The basic parameters of the turbine used in this text are given in Table 1. Figure 1d shows the structure of the turbine with the WEGS proposed in this work, which has five parameters: the length of the shrinkage and diffusion tube L_1, the length of the centerboard L_2, the length of the throat L_3, the length of the wind board L_4, and the shrinkage and diffusion angle α (to simplify the study, the length and the angle of the shrinkage tube are same as those of the diffusion tube); the subsequent work will start with the optimization of these five parameters.

Table 1. Parameter values of the studied turbine.

Parameter	Value
Number of blades	2
Thickness of blades (mm)	2
H (m)	1
D (m)	0.909
d (m)	0.5
D_R (m)	0.999
S (m)	0.091
e (S/d)	0.182
v (m/s)	7

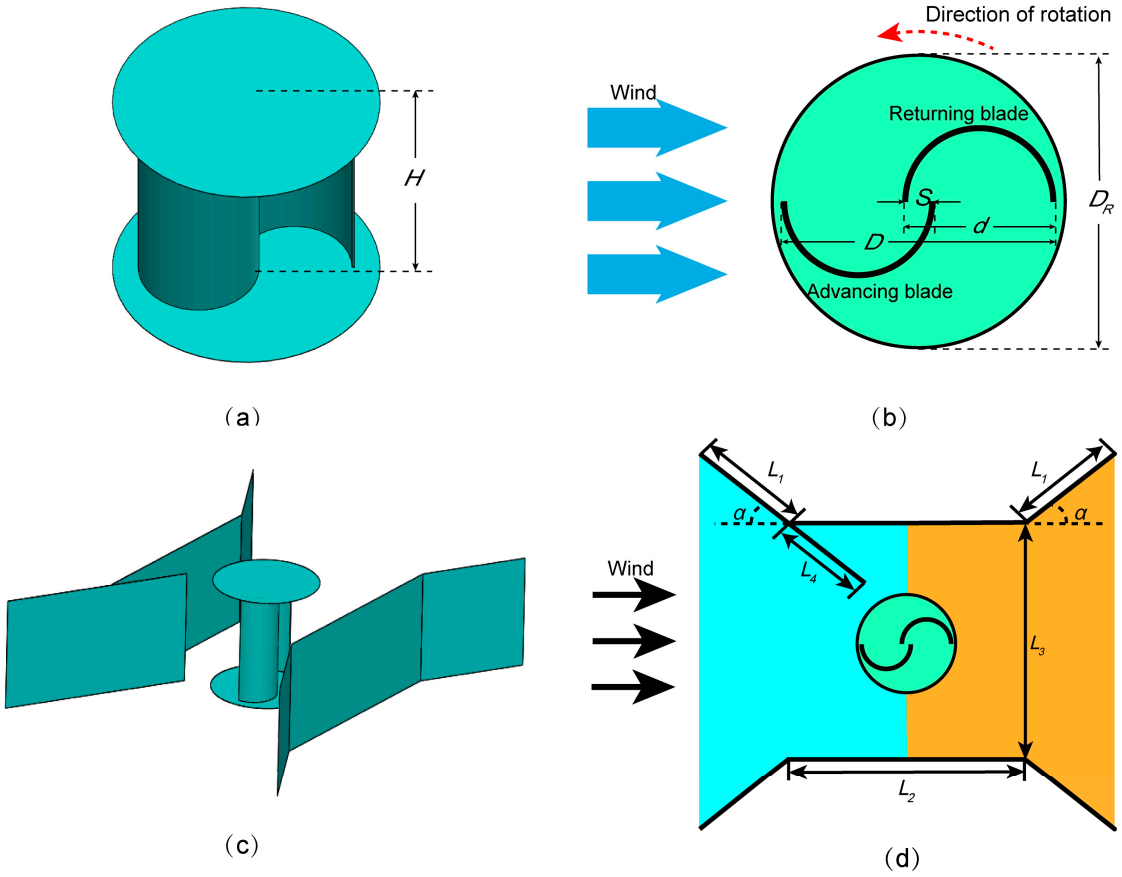


Figure 1. Schematic of Savonius wind turbine and the WEGS: (**a**) 3D schematic of the turbine; (**b**) 2D schematic of the turbine; (**c**) 3D diagram of the WEGS; (**d**) 2D diagram of the WEGS.

2.2. Performance Indicators

The power coefficient C_p and the torque coefficient C_t are used to measure the wind-trapping capacity of the turbine. C_t and C_p are given by Equations (1) and (2) [29]:

$$C_t = \frac{T}{0.25\rho A {v_\infty}^2 D} = \frac{T}{0.25\rho D^2 H {v_\infty}^2} \tag{1}$$

$$C_p = \frac{P}{0.5\rho A {v_\infty}^3} = \frac{P}{0.5\rho D H {v_\infty}^3} \tag{2}$$

where T represents the turbine torque, P stands for the turbine power, ρ indicates the air density, A represents the swept area of the turbine, D refers to the diameter of the turbine, v indicates the wind speed, and H stands for the height of the turbine. C_p and C_t are closely related, and the connection between them is given by the following equation:

$$C_p = \lambda \cdot C_t \tag{3}$$

where λ is also known as the tip speed ratio (TSR) and is given by Equation (4) [30]:

$$TSR = \frac{R\omega}{v_\infty}, \tag{4}$$

where R stands for the turbine radius and ω represents the angular velocity of the turbine. In this work, the values of C_p and C_t are obtained with TSR = 1, and both have the same value according to Equation (3).

3. Computational Fluid Dynamics Simulation

CFD is widely used in similar studies and has a high degree of accuracy [31,32]. Therefore, in this research, CFD is employed to study the effect of the design parameters on the performance of the WEGS. In addition, 3D simulation is more accurate than 2D simulation, but the high cost of time and resources is its weakness [33,34]. In previous studies of auxiliary structures, 2D simulations have been shown to be sufficiently accurate [21,25,35]. Therefore, considering the cost of the time, 2D CFD simulation is employed in this study, and the 2D models in this section are all for the first set of tests in the orthogonal table (the relevant data are given in Section 4). The main assumptions made for the 2D simulations in this paper are that the height of the WEGS is the same as that of the turbine, ignoring energy losses as well as temperature variations

3.1. Calculation Domain Settings

The 2D computational domain of the turbine with the WEGS is demonstrated in Figure 2. CFD simulations are performed through ANSYS FLUENT 2019 R2, and the computational domain is split into a stationary domain and a rotational domain by a sliding interface. The turbine's rotational motion is executed by the rotational domain, which has a determined size of 1.1D. The left inlet is the velocity inlet (v = 7 m/s), the viscosity of the air is 1.7894 $\times$ 10^{-5} kg/m.s, the density of the air is 1.225 kg/m^3, and the Reynolds number is 4.32 $\times$ 10^5. The right outlet is a pressure outlet with the same pressure value as the atmospheric pressure. The upper and lower walls are set up as symmetry boundaries, and both the advance and return blades are set up as no-slip walls. The SIMPLE method is used to solve the Navier–Stokes equations describing the conservation of momentum for incompressible viscous fluids. Furthermore, the SST k-ω model has been proven by many researchers to be able to accurately analyze the flow field; therefore, it is identified as the turbulence model for this work [36–38].

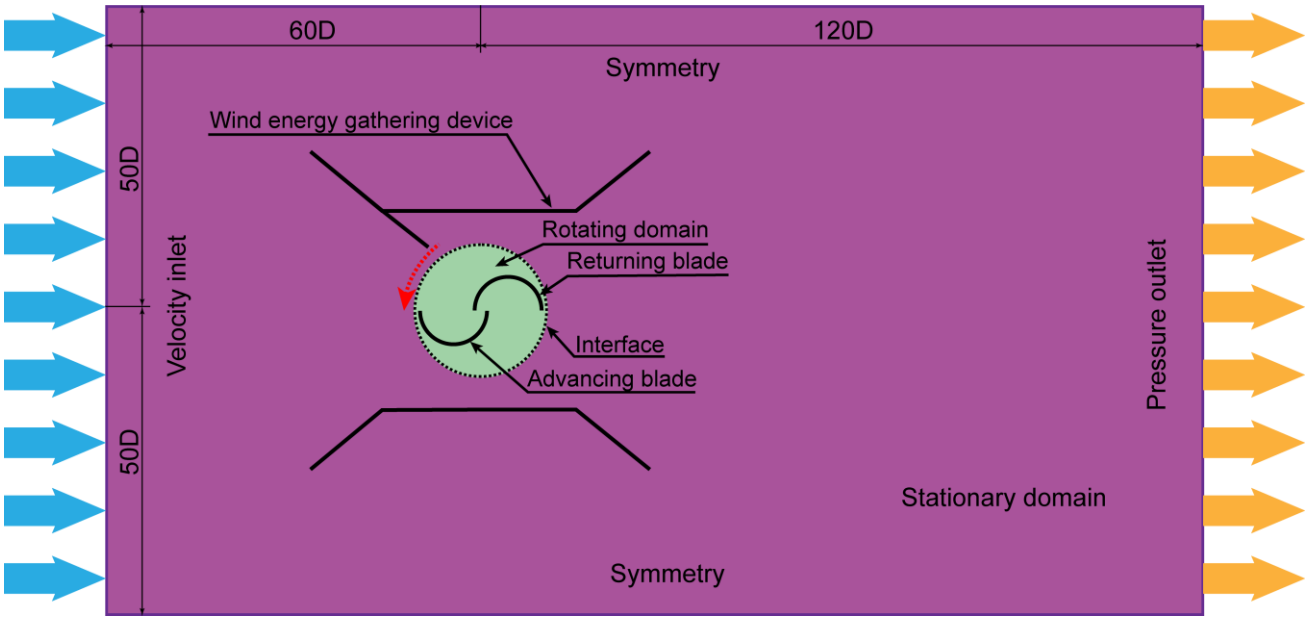


Figure 2. Computational domain of the Savonius wind turbine with the WEGS.

The size of the domain has a momentous influence on the simulation results of C_t and C_p, so domain independence analysis is needed to guarantee the accuracy of the simulation. In this work, the size of six different domains, i.e., 20D $\times$ 30D(A), 30D $\times$ 60D(B), 60D $\times$ 90D(C), 80D $\times$ 120D(D), 100D $\times$ 180D(E), 120D $\times$ 240D(F) are investigated, and the data obtained are shown in Figure 3. Figure 3 shows that C_t tends to stabilize after the domain reaches 80D $\times$ 120D. The differences in C_t of the 100D $\times$ 180D domain compared

to the $80D \times 120D$ domain and the $120D \times 240D$ domain is 0.28% and 0.66%, respectively, which are very close in value, so the domain size of the subsequent work in this study is set at $100D \times 180D$(E).

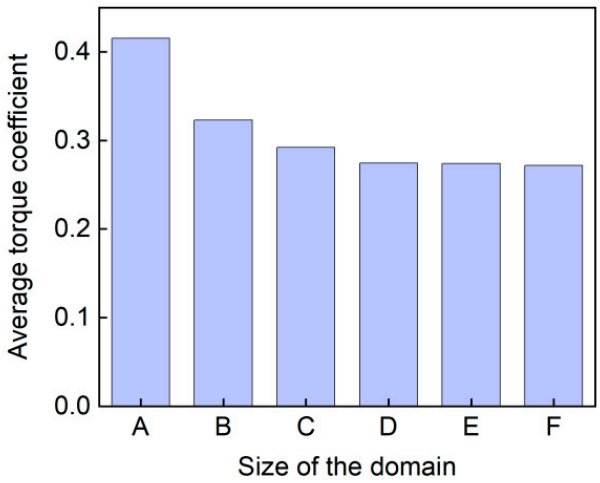


Figure 3. C_t of different domains of trial 1 in the orthogonal table.

3.2. Division of the Grid

Mesh delineation is the basis for performing CFD simulations. A coarse mesh will affect the accuracy of C_t, and a mesh that is too fine will waste a lot of computing time, so it is especially important to generate a reasonable mesh using mesh independence verification. In this work, three different sets of grids with grid numbers of 149,645, 327,842, and 571,853, respectively, are selected, and the results of the C_t of the turbine in one cycle obtained by these three sets of grids are demonstrated in Figure 4. This figure demonstrates that the C_t values of the set with 327,842 grids and the set with 571,853 grids are very similar. The thickness of the first layer of the mesh at the solid wall is determined to be 0.025 mm, the number of layers is determined to be 20, and the growth rate is determined to be 1.2. Meanwhile, the meshes near the boundary and in the rotation domains are locally refined. Figure 5 shows the final result of the grid segmentation.

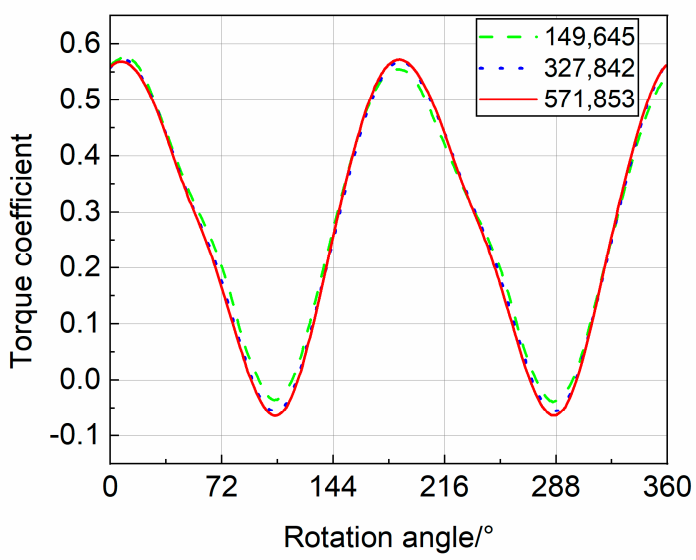


Figure 4. Mesh independence study.

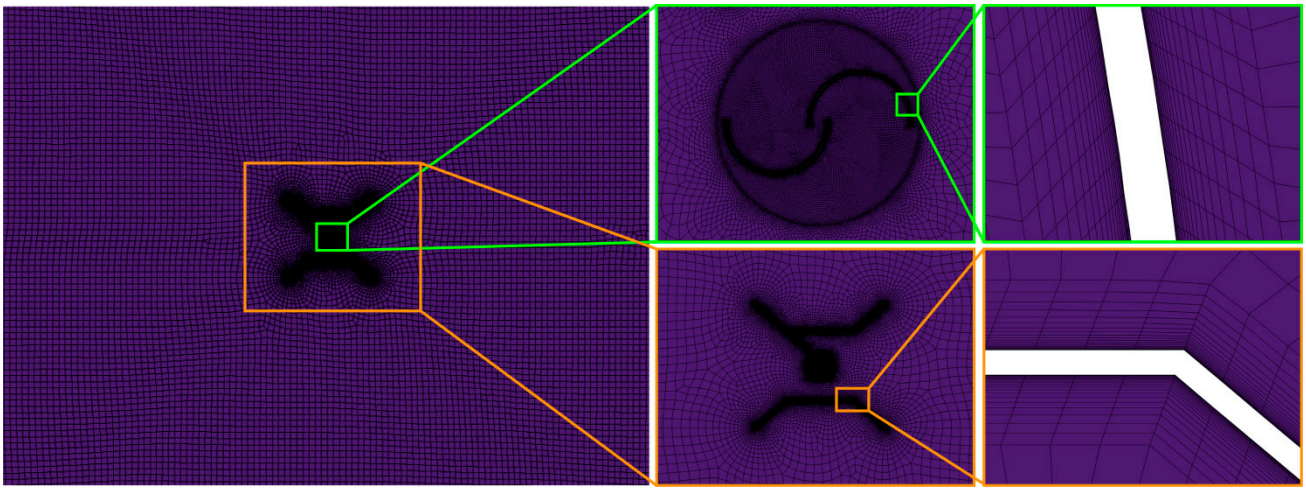


Figure 5. Savonius wind turbine mesh division details.

3.3. Selection of Time Step

Another momentous factor affecting the accuracy of the final simulation results is the time step. And its calculation formula is as follows:

$$\Delta t|_{\theta^\circ} = \frac{\theta}{\omega \frac{180}{\pi}}, \tag{5}$$

where θ refers to the increment in the azimuthal angle in one time step and ω indicates the angular velocity of the rotor. By dividing the azimuthal increments into 0.5°/step, 1°/step, 1.5°/step, 2°/step, 3°/step, and 4°/step and performing CFD simulations, the difference in the simulated C_t value of each azimuthal increment compared to the previous increment was demonstrated, as shown in Figure 6. It can be found that the C_t values of 0.5°/step, 1°/step, and 1.5°/step are very close to each other, and considering both accuracy and computation time, 1°/step is chosen as the azimuth increment for this work. In addition, the time step value for each rotation angle is 0.0011332173503.

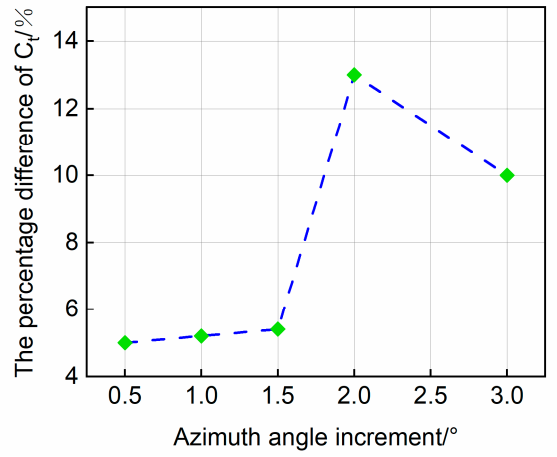


Figure 6. Percentage difference in azimuthal increments relative to the previous one.

After the determination of the grid-independence verification as well as the time-step-independence verification, the size of y^+ determines the reliability of the overall simulation results. The SST k-ω turbulence model must ensure that the y^+ value of the solid wall surface is less than 1. Therefore, it is necessary to determine the y^+ case of the solid wall surface of the entire mesh set to ensure the accuracy of the results of the subsequent calculations. In this set of grids, the open turbine has a maximum y^+ = 0.716 and an average

$y^+ = 0.23$, and the WEGS has a maximum $y^+ = 0.976$ and an average $y^+ = 0.1797$ to accurately capture turbulence features near the surface of the solid wall. The airfoil surface y^+ case is shown in Figures 7 and 8.

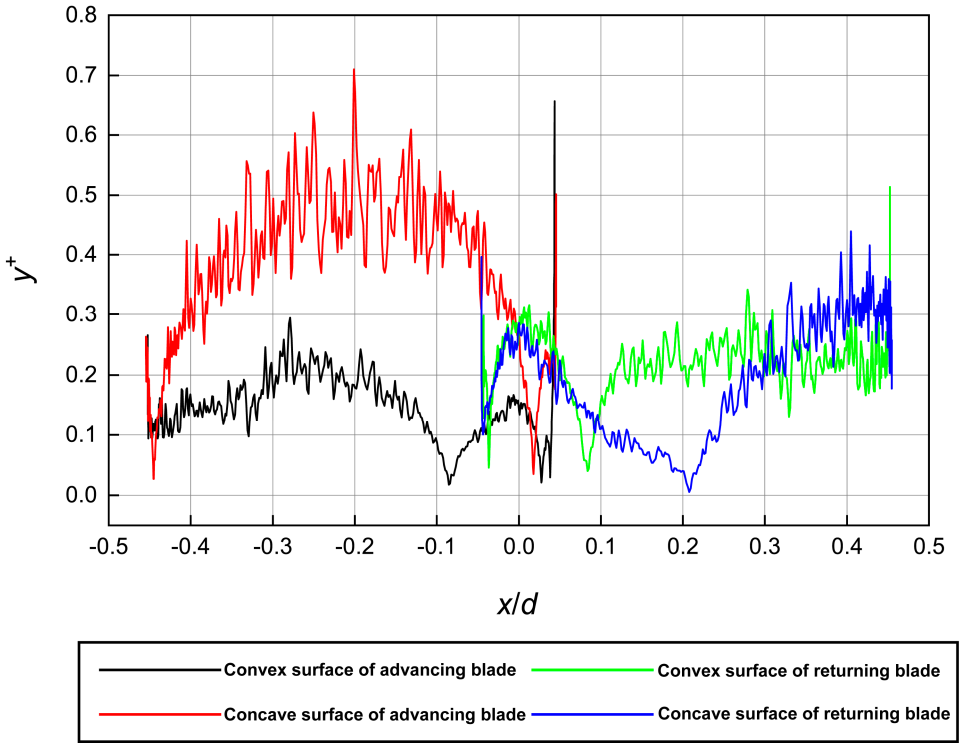


Figure 7. Distribution of y^+ around wind turbine blades.

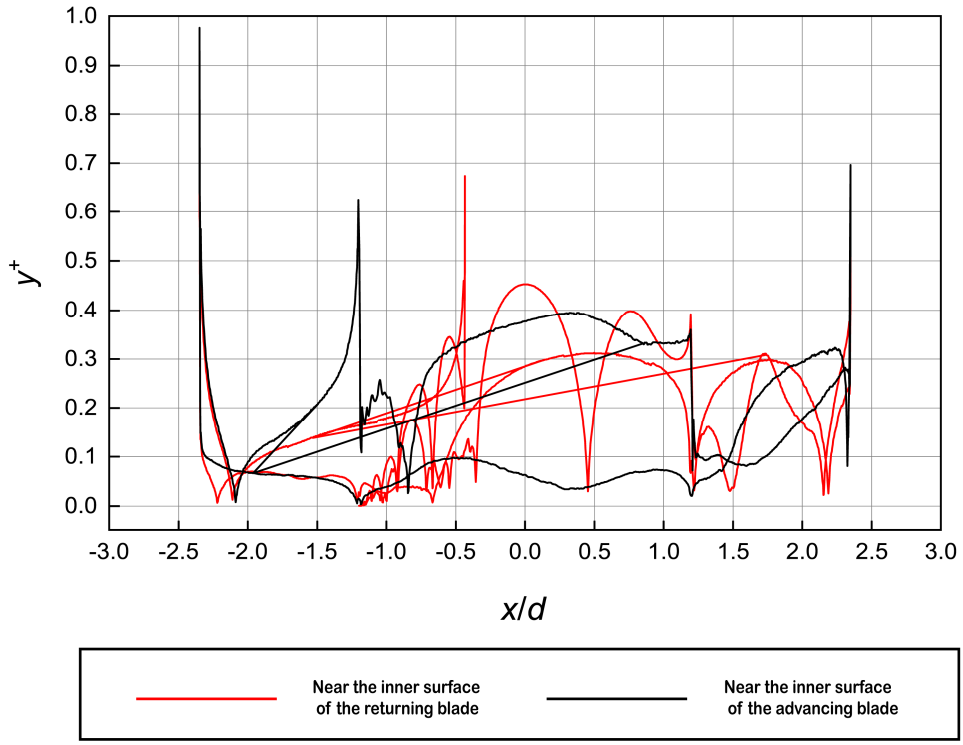


Figure 8. Distribution of y^+ around WEGS.

3.4. Verification of Accuracy

When conducting the CFD simulation, it is necessary to simulate the turbine through continuous multiple rotations to ensure that the simulation results reach convergence. For example, Figure 9 demonstrates the *Ct* values of the turbine with the WEGS corresponding to test 1 of the orthogonal experiment given in the following text at *TSR* = 1 through 30 continuous rotations. From this figure, it can be seen that the results are gradually converging as the simulation progresses, and the difference between the last two rotations is only 0.16%. Therefore, in the following work, the performance of the turbine is evaluated using the C_t of the last cycle.

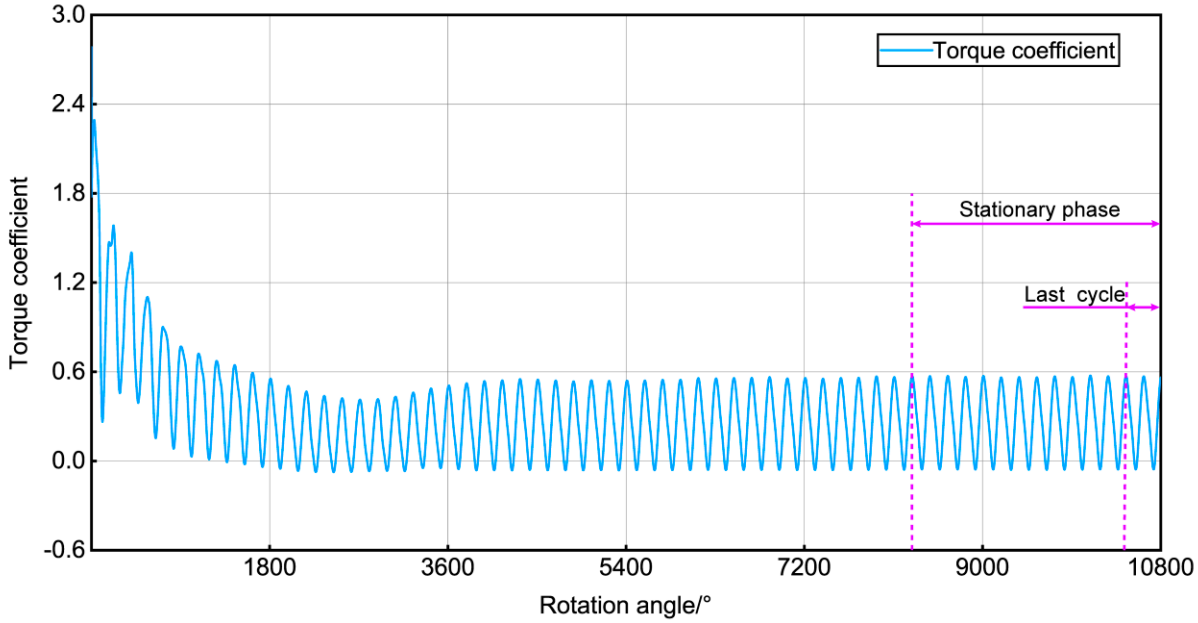


Figure 9. Instantaneous C_t values for 30 rotational cycles of test 1 in the orthogonal table at *TSR* = 1.

To illustrate the accuracy of the CFD simulation mentioned above, the open turbine (without the WEGS) is simulated and compared with the experimental data [28], and the results obtained are demonstrated in Figure 10. Figure 10 demonstrates the good fit of the simulation results to the experimental results within the range of *TSR* = 0.6–1.2, especially in the range of *TSR* = 0.9–1.2, so it is feasible to predict the performance enhancement of the turbine with the WEGS by the present CFD simulation environment.

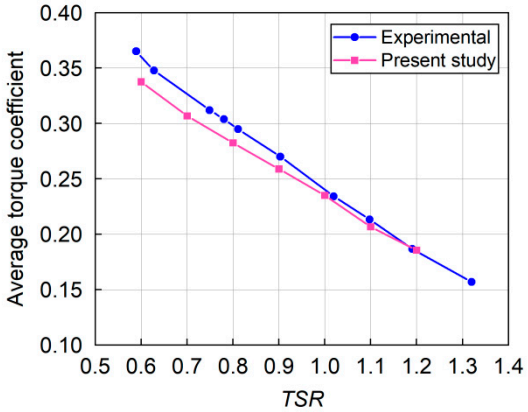


Figure 10. Comparison between the present research work and the experimental data of Sheldahl et al. [28].

4. Taguchi Experiments on Structural Parameters

Taguchi's method is used to investigate the impact of the structure parameters of the WEGS in this study. Firstly, an orthogonal table with five factors and three levels is used to arrange 18 combinations of the different parameters of the WEGS, and CFD is used to evaluate their performance. Then, the order of significance of these factors is found by ANOVA. Finally, the signal-to-noise ratio of the optimal combinations predicted by Taguchi's method is compared with that of the optimal combinations simulated by CFD to examine the accuracy of the method.

4.1. Taguchi's Method

Taguchi's method is extremely widely used in the research field due to the fact that it can find the best combination of the different factors with fewer trials [39]. In the study of VAWT, the prediction of Taguchi's method also plays an important role and has shown a good performance [2,40–42].

The selection of structural parameters and levels is first carried out. In this work, five important parameters of the WEGS as shown in Figure 1c are investigated, namely the length of the shrinkage and diffusion tubes L_1, the length of the centerboard L_2, the length of the throat L_3, the length of the wind board L_4, and the shrinkage and diffusion angle α. Three levels are selected for each parameter, and the detailed parameters are presented in Table 2.

Table 2. The level setting for each structural parameter.

Factor	Level 1	Level 2	Level 3
A: the length of the shrinkage and diffusion tubes (L_1) (mm)	1200	1350	1500
B: the length of the centerboard (L_2) (mm)	2400	2500	2600
C: the length of the throat (L_3) (mm)	2400	2500	2600
D: the length of the wind board (L_4) (mm)	900	950	1000
E: the shrinkage and diffusion angle (α) (°)	30°	35°	40°

After the determination of the appropriate structural parameters and design levels, the selection of orthogonal tables follows. Orthogonal tables are neatly comparable and uniformly dispersed and can achieve full experimental results with a small number of trials [43]. The basic requirement for choosing an orthogonal table is that the sum of the degrees of freedom of each structural parameter should be less than the total degrees of freedom [44]. Therefore, L18 (3^5) is selected as the orthogonal table for this work. This table has a total of 17 degrees of freedom, and the total of the degrees of freedom of each structure parameter is 10, which can satisfy the requirements of the subsequent analysis work. L18 (3^5) is presented in Table 3.

Table 3. L18 (3^5) orthogonal table.

Case	A	B	C	D	E
1	1	1	1	1	1
2	1	1	2	2	3
3	1	2	1	3	3
4	1	2	3	1	2
5	1	3	2	3	2
6	1	3	3	2	1
7	2	1	1	3	2
8	2	1	3	1	3
9	2	2	2	2	2
10	2	2	3	3	1
11	2	3	1	2	3
12	2	3	2	1	1
13	3	1	2	3	1
14	3	1	3	2	2
15	3	2	1	2	1
16	3	2	2	1	3
17	3	3	1	1	2
18	3	3	3	3	3

4.2. Analysis of Variance (ANOVA)

ANOVA can be performed on the test data obtained by Taguchi's method to determine the significance of the effect of each structural parameter on the average C_p and find which parameters are statistically significant [45]. When analyzing data using ANOVA, the calculation of the sum of squares of the deviations is an indispensable and crucial step, whose equation is shown as follows:

$$S_T = \sum_{i=1}^{n} (y_i - \overline{y})^2, \tag{6}$$

$$S_j = \frac{n}{a} \sum_{k=1}^{n} (\overline{y_{jk}} - \overline{y})^2, \tag{7}$$

$$S_e = S_T - S_j, \tag{8}$$

where S_T refers to the total of squares of total deviations, S_j represents the total of squares of deviations for each factor, S_e indicates the total of squares of errors, n is the number of trials, a represents the number of levels for each factor, y_i indicates the mean C_p of each trial, $\overline{y}$ is the average of the mean C_p for all trials, and $\overline{y_{jk}}$ is the average C_p corresponding to factor j at k levels. The F-test, also known as the variance ratio test, is suitable for analyzing statistical models with multiple factors [46]. The formula of the F-test in this paper is as follows:

$$F = \frac{MS_j}{MS_e} = \frac{S_j / f}{S_e / (n-1) - 5f}, \tag{9}$$

where MS_j indicates the mean square of each factor, MS_e indicates the mean square of the error, and f refers to the degrees of freedom $(a - 1)$ of each factor. For the calculation of the p-value, it is generally realized by the FDIST function.

4.3. Best Combination Prediction

Taguchi's method utilizes the signal-to-noise (S/N) ratio to find the optimal level of each parameter and to predict the test results corresponding to the combination of them [2]. S/N scores are of three types: lower is better, closer to the target is better, and bigger is better [47]. The type used in this study is "bigger is better" to maximize the C_p of the turbine, which is defined as follows [40]:

$$S/N = -10log\left[\left(\frac{1}{y_i}\right)^2\right], \tag{10}$$

The optimal levels of the different factors are combined together to form the optimal test scheme. Then, Taguchi's method uses Equation (11) to predict the signal-to-noise ratio for this test scenario [48]. Then, by substituting the predicted S/N back to Equation (10), the predicted average C_p of the turbine can be obtained. It is then examined by simulation (CFD) to verify the accuracy of the present optimization method.

$$\begin{aligned} S/N_{predict} = \quad & \overline{S/N} + (S/N_{Af} - \overline{S/N}) + (S/N_{Bg} - \overline{S/N}) + (S/N_{Ch} - \overline{S/N}) \\ & + \left(S/N_{Di} - \overline{S/N}\right) + \left(S/N_{Ej} - \overline{S/N}\right) \end{aligned} \tag{11}$$

where *Af*, *Bg*, *Ch*, *Di*, and *Ej* are the optimal levels of each structural parameter.

5. Results and Discussion

5.1. Results of Taguchi and ANOVA Analyses

Table 4 demonstrates the mean C_p of the 18 test sets in the orthogonal table, the average C_p growth rate compared to the open turbine, and the S/N ratio. Table 4 clearly shows that at *TSR* = 1, the wind-trapping capacity of all 18 test sets is better than that of the open

turbine, with an average S/N ratio of −10.7283 and an average C_p of 0.2914. The best one in the orthogonal table is Trial Group 18, i.e., $A_3B_3C_3D_3E_3$, which has an average C_p of 31.74 (about 35% higher than the open turbine) and a signal-to-noise ratio of −9.97. Even the worst one, i.e., Trial Group 6 ($A_1B_3C_3D_2E_1$), also results in an increase in the average C_p of the wind turbine by 9.83%. The current work yields the surprising result that even the worst WEGS structure can still improve the turbine performance relatively substantially.

Table 4. Simulation results of 18 sets of data in the orthogonal table.

Case	L_1	L_2	L_3	L_4	α	Mean C_p	Improvement of Average C_p	S/N Ratio
1	1200	2400	2400	900	30°	0.2737	16.4%	−11.25
2	1200	2400	2500	950	40°	0.3094	31.6%	−10.19
3	1200	2500	2400	1000	40°	0.3105	32.1%	−10.16
4	1200	2500	2600	900	35°	0.2795	18.9%	−11.07
5	1200	2600	2500	1000	35°	0.2732	16.2%	−11.27
6	1200	2600	2600	950	30°	0.2582	9.83%	−11.76
7	1350	2400	2400	1000	35°	0.2942	25.1%	−10.63
8	1350	2400	2600	900	40°	0.3156	34.2%	−10.02
9	1350	2500	2500	950	35°	0.2992	27.3%	−10.48
10	1350	2500	2600	1000	30°	0.2795	18.9%	−11.07
11	1350	2600	2400	950	40°	0.2852	21.3%	−10.9
12	1350	2600	2500	900	30°	0.2666	13.4%	−11.48
13	1500	2400	2500	1000	30°	0.3026	28.7%	−10.38
14	1500	2400	2600	950	35°	0.3018	28.4%	−10.41
15	1500	2500	2400	950	30°	0.2702	14.9%	−11.37
16	1500	2500	2500	900	40°	0.3143	33.7%	−10.05
17	1500	2600	2400	900	35°	0.2935	24.8%	−10.65
18	1500	2600	2600	1000	40°	0.3174	35%	−9.97

The data in Table 4 are analyzed by ANOVA to find the key parameters that affect the performance of the turbine and whether each parameter is statistically significant for C_p. The ANOVA results are demonstrated in Table 5, which indicates that the order of these parameters affecting the performance of C_p is E > B > A > D > C and A, B, and E are statistically significant.

Table 5. ANOVA results for each structural parameter.

Factor	*S*	*f*	*MS*	*F*	*P*	Significance
A	0.00077	2	0.00039	5.6095	0.0352	<0.05
B	0.00089	2	0.00045	6.4905	0.0254	<0.05
C	0.00012	2	0.00006	0.9001	0.4489	>0.05
D	0.00024	2	0.00012	1.7710	0.2386	>0.05
E	0.00340	2	0.00170	24.6793	0.0007	<0.05
ERROR	0.00048	7	0.00007			

5.2. Predicted and Simulated Values

The average signal-to-noise ratio at different levels for each structural parameter is given in Figure 11. Since here a higher S/N ratio represents a better performance of the wind turbine, Figure 11 demonstrates that the optimal combination of the parameter levels is $A_3B_1C_2D_3E_3$.

The best combination is predicted by Equation (11) and compared with the CFD simulation results, and the final results are arranged in Table 6. Table 6 demonstrates that the predicted mean C_p (0.3361) is extremely close to that given by the CFD simulations (0.3341), with a difference of only 0.6%, thus showing the reliability of the presented method. Compared with the open turbine and the best trial in the orthogonal table (Case18),

the average C_p of the best combination $A_3B_1C_2D_3E_3$ is improved by 42.1% and 5.3%, respectively, indicating a significant improvement in the wind-trapping capacity.

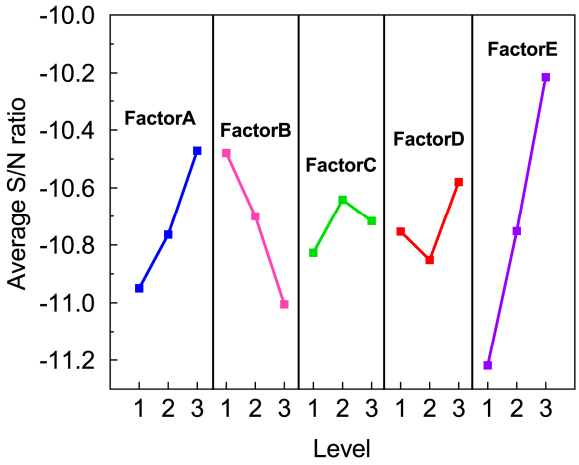


Figure 11. Average S/N ratio for different levels of each structural parameter.

Table 6. Comparison of predicted and simulated values.

Levels	Average C_p	S/N Ratio
$A_3B_3C_3D_3E_3$ (Case18)	0.3174	−9.97
$A_3B_1C_2D_3E_3$ (Prediction)	0.3361	−9.47
$A_3B_1C_2D_3E_3$ (CFD)	0.3341	−9.52

5.3. Performance Analysis

A comparison of the mean C_t and C_p of the turbine with the best WEGS ($A_3B_1C_2D_3E_3$) and the open turbine in the TSR = 0.6–1.2 range is given in Figure 12. It is clear from the figure that the turbine with the best WEGS performs much better than the open turbine in the selected range, with enhancements ranging from 20.1% to 53%. These results fully demonstrate the enhancement of the WEGS in the wind-trapping capacity of the turbine.

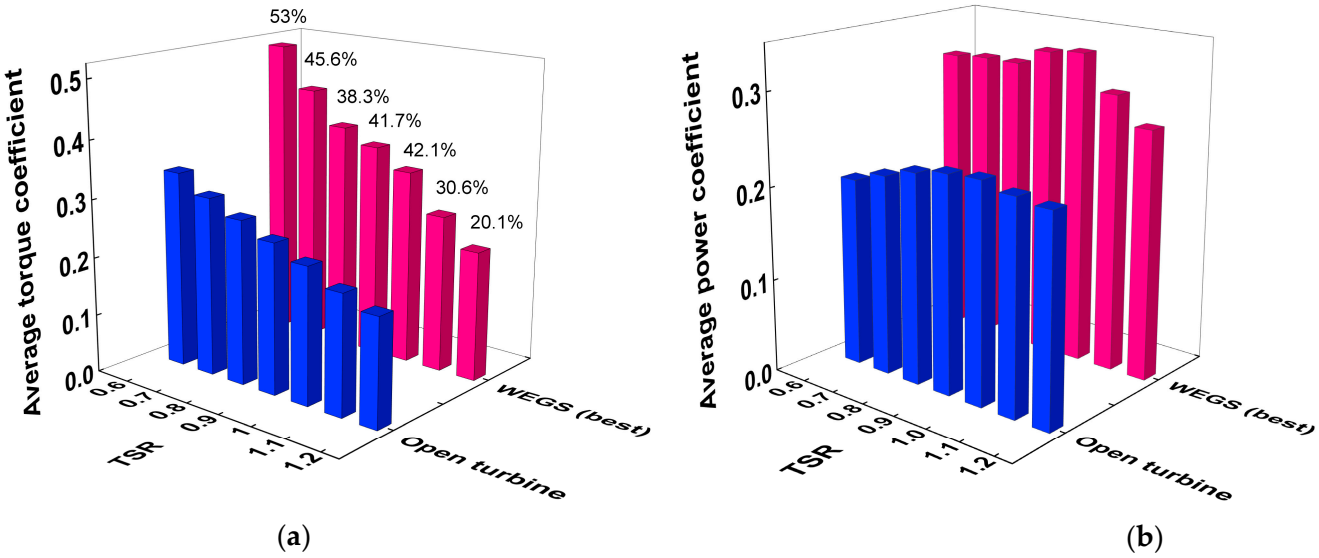
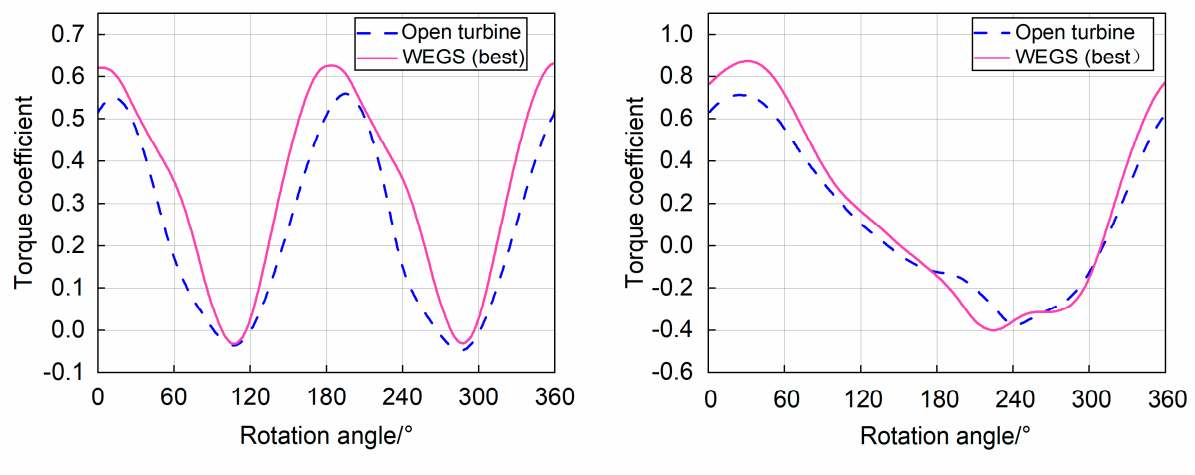


Figure 12. Performance comparison of the turbine with the best WEGS and the open turbine at different *TSRs*. (**a**) C_t values. (**b**) C_p values.

The instantaneous C_t of the turbine with the best WEGS and the open turbine over one cycle at TSR = 1 is shown in Figure 13. Figure 13a demonstrates the variation in the transient C_t of the whole turbines, and it can be seen that compared with the open turbine, the transient C_t of the turbine with the best WEGS improves in all ranges from 0° to 360°; especially when approaching the upper peak, the improvement of transient C_t is more obvious, and even at the lower peak, the transient C_t of the turbine with the best WEGS is higher than that of the open turbine. A single blade is a good representation of the change in instantaneous C_t as the blade advances and returns, so the instantaneous C_t of a single blade is given in Figure 13b. It is evident that the turbine with the best WEGS outperforms the open turbine at 0–180° in the advance process and at 240–260° and 310–360° in the return process, but it performs slightly worse than the open turbine at 180–240° and 260–310°. All in all, though the WEGS weakens the energy capture ability of the blade at some individual positions during the return process, from the perspective of the entire rotation cycle, it still significantly improves the energy capture capacity of the turbine.



(**a**) (**b**)

Figure 13. Difference in instantaneous C_t values at TSR = 1: (**a**) Savonius wind turbine, (**b**) single blade.

To better demonstrate the performance of the turbine with the best WEGS compared to the open turbine at the remaining *TSRs*, we analyze the instantaneous C_t of the remaining *TSRs*, as demonstrated in Figure 14. By combining Figures 13 and 14, it can be found that the instantaneous C_t of the turbine with the best WEGS is larger than that of the open turbine in the range of TSR = 0.6–1. At TSR = 1.1–1.2, although the instantaneous C_t of the turbine with the best WEGS is slightly lower than that of the open turbine in individual positions, it is much higher than the instantaneous C_t of the open turbine in the vast majority of rotational positions.

Furthermore, the average C_t values of the turbine with the best WEGS and the open turbine at wind speeds of 5 m/s, 6 m/s, 8 m/s, and 9 m/s and TSR = 0.6–1.2 are also compared and studied, and the results are demonstrated in Figure 15. Figure 15 demonstrates that the turbine with the best WEGS always holds significant advantages over the open turbine at all the investigated wind speeds and *TSRs*.

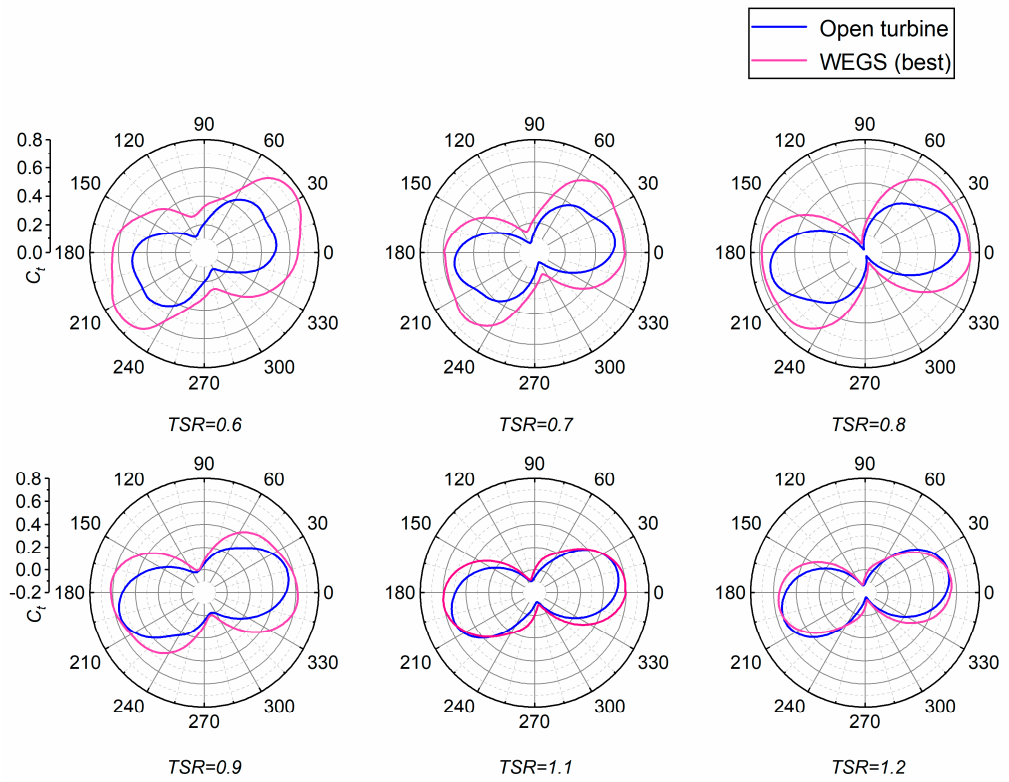


Figure 14. Instantaneous torques for the remaining *TSR* in the study range.

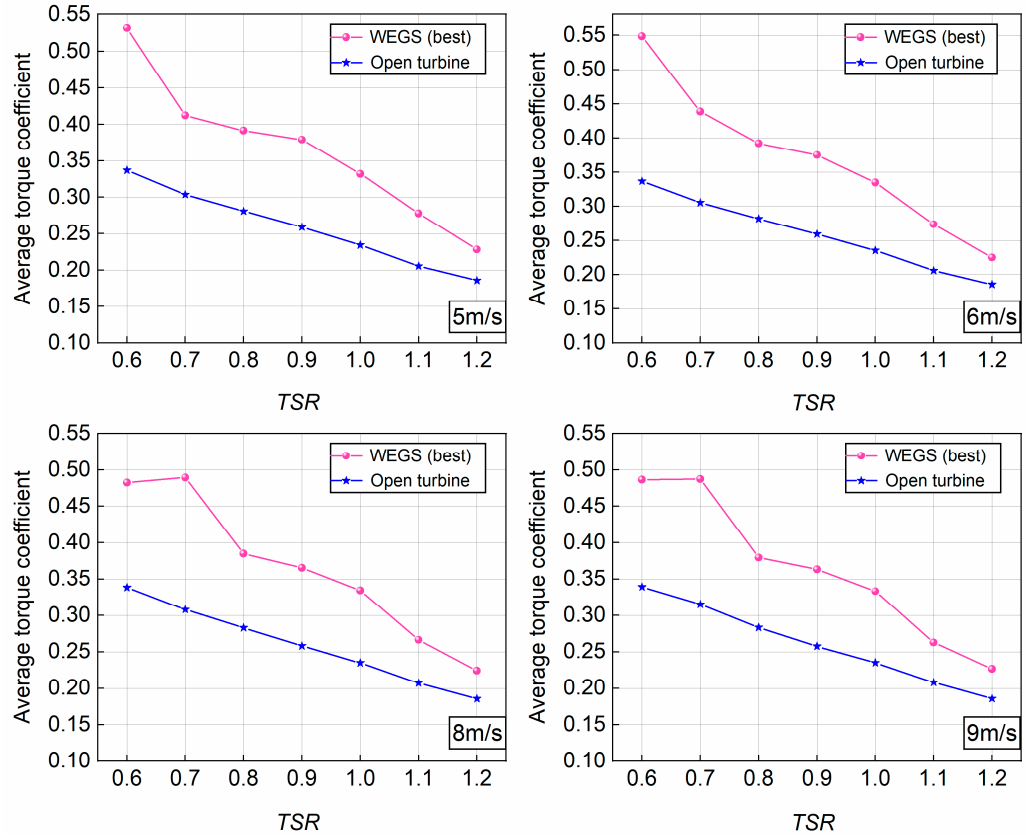


Figure 15. Average torque coefficients of the turbine with the best WEGS and the open turbine at other wind speeds (*TSR* = 0.6–1.2).

5.4. Torque Ripple Factor (TRF)

TRF is a measure of the fluctuations in turbine torque during a steady-state cyclic flow and is related to the life of the turbine [31,49]. The lower the *TRF*, the lower the fluctuations and the longer the life of the turbine. The calculation of *TRF* is given by Equation (12):

$$TRF = \frac{C_{t,max} - C_{t,min}}{C_t} \tag{12}$$

where $C_{t,max}$ and $C_{t,min}$ are the maximum and minimum instantaneous torque coefficients in one cycle, respectively, and C_t is the average torque coefficient. The *TRFs* of the open turbine and the turbine with the best WEGS under each *TSR* are given in Figure 16. It can be seen that the *TRF* of the turbine with the best WEGS is lower than that of the open turbine for the range of *TSR* studied, indicating that the turbine with the best WEGS suffers less fluctuation during the rotation process and has a longer service life.

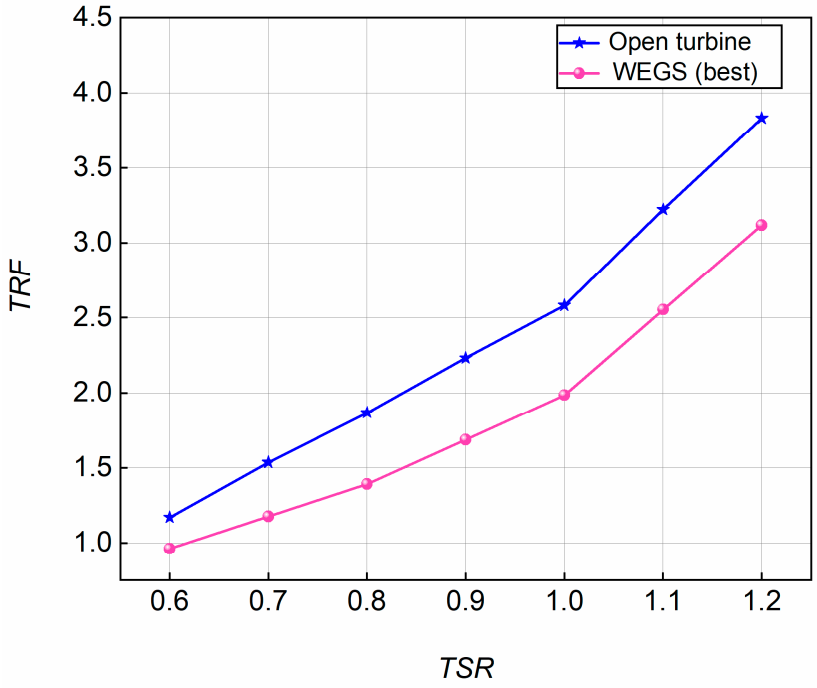


Figure 16. *TRF* of the turbine with the best WEGS and the open turbine.

5.5. Flow Field Analysis

There are two processes that occur in a single rotation cycle of the individual blades of a turbine: the advance process from 0° to 180° and the return process from 180° to 360°, where the advance blade becomes a return blade at 180° and the return blade becomes an advance blade at 360°. From Figure 13, it can be found that at 180° and 360°, the instantaneous C_t of the turbine is close to the upper peak, and at 90° and 270°, the instantaneous C_t of the turbine is close to the lower peak. Therefore, in the following paragraphs, these four positions will be used as representatives to illustrate the advantages of the WEGS. For ease of understanding, the blades studied at rotation positions of 90° and 360° are defined as the advance blade, and the blades studied at rotation positions of 180° and 270° are defined as the return blade. The concave surface of the advance blade and the convex surface of the return blade are the windward surface of the blade, and the remaining portions are the leeward surface of the blade.

The pressure distributions of the open turbine and the turbine with the best WEGS at 90° are demonstrated in Figure 17. As shown in Figure 17a, at the 90° rotation position, a very distinct low-pressure area (LPA) is formed near the advance blade's tip. This is caused by the airflow on the windward surface of the advance blade meeting the upstream airflow In conjunction, Figures 17 and 18 demonstrate that the shrinkage tubes and the wind board of the WEGS make it easier for the airflow from the windward surfaces of the advancing blades to converge with the upstream airflow, resulting in stronger vortices at the blade tips and creating more pronounced areas of low pressure [35]. This phenomenon is also explained by Figure 19a, where the open turbine has a similar windward pressure as the turbine with the best WEGS, but on the leeward surface, the pressure of the turbine with the best WEGS is much lower than that of the open turbine, and therefore, at a rotational angle of 90°, the turbine with the best WEGS develops a much larger pressure difference than the open turbine, which greatly enhances the positive torque of the advance blade.

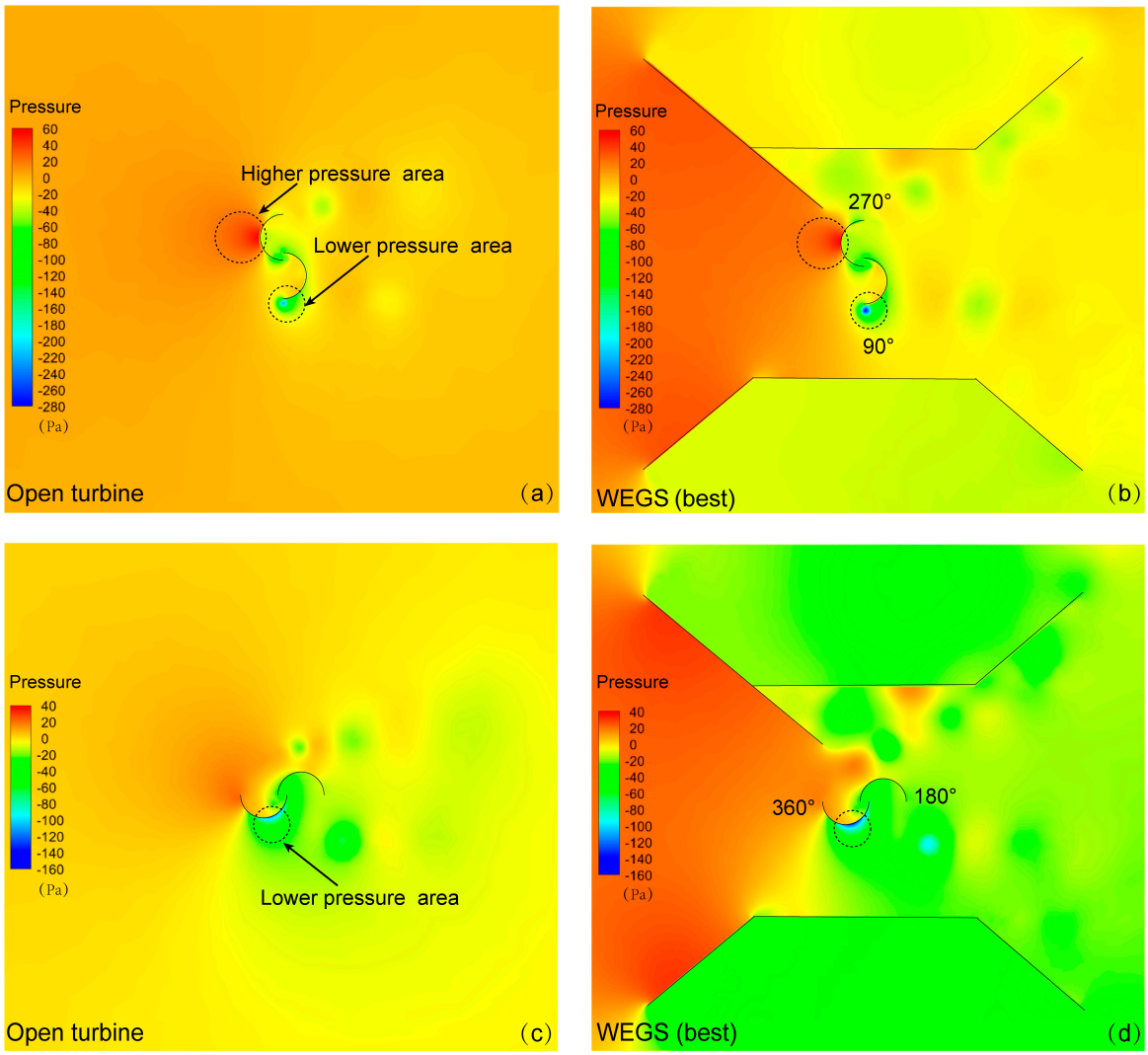


Figure 17. Pressure distribution near upper and lower peaks for the open turbine and the turbine with the best WEGS (*TSR* = 1).

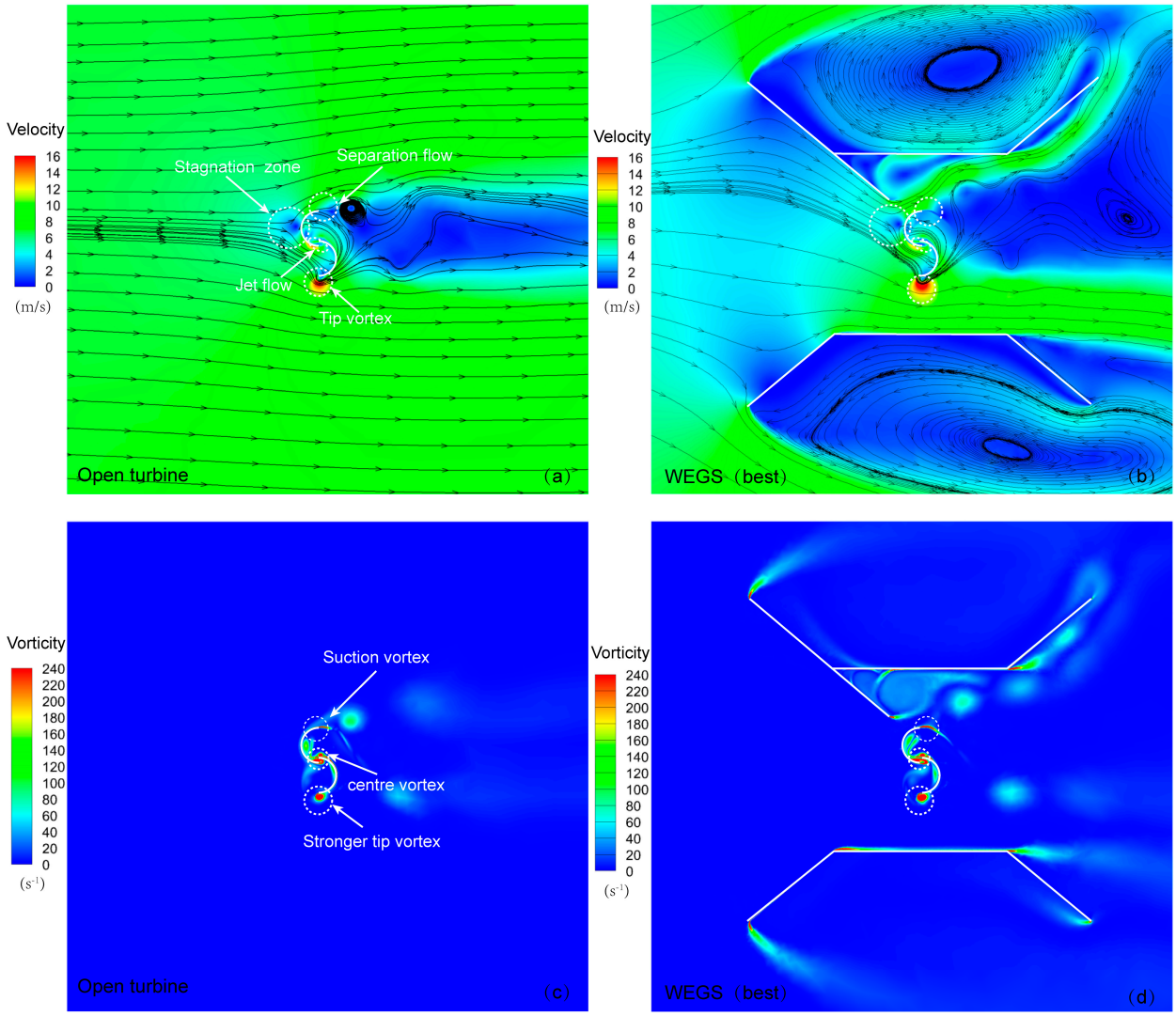


Figure 18. Velocity versus vortex plots for the open turbine and the turbine with the best WEGS at rotation position 90° and 270° (*TSR* = 1).

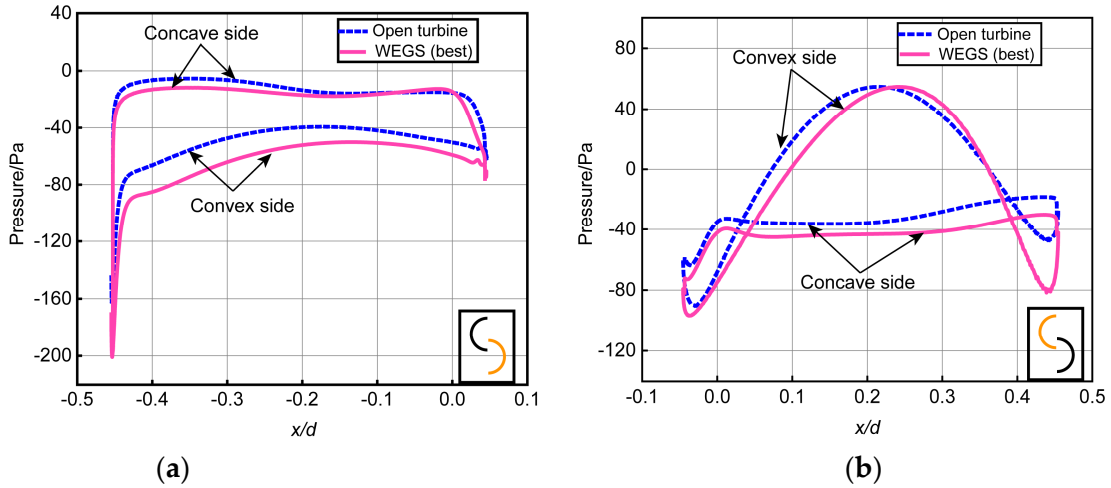


Figure 19. Surface pressure diagrams of open turbine and WEGS (best) blades at *TSR* = 1: (**a**) 90°; (**b**) 270°.

From Figure 17c,d, it can be observed that when the rotational angles of the two blades are 0° and 180°, respectively, the WEGS makes the pressure on the concave side of the advance blade greater and makes the LPA on the convex side of the advance blade more obvious; both of these are conducive to the rotation of the blade, and thus, the turbine with the WEGS shows better performance at this position.

When the rotational position reaches 270°, a stagnation zone is created at the front of the return blade. When we combine Figure 17a,b, Figures 18 and 19b, it is evident that the turbine with the best WEGS has a smaller stagnation zone than the open turbine. In addition, as can be seen from Figure 19b, when $x/d > 0.4$, the pressure on the convex side of the return blade is less than that on its concave side. This point is conducive to the rotation of the blade. Meanwhile, after the WEGS is added, the pressure difference between the concave and the convex side of the return blade is larger. Both of these have positive contributions to the weakening of negative torque. On the other hand, it can also be seen from Figure 19b that a stronger suction vortex appears on the concave side of the return blade of the turbine with the WEGS. According to [35], this phenomenon is caused by a stronger jet flow (airflow between the two blades) and separation flow (airflow at the tip of the return blade) and leads to a stronger LPA on the leeward surface of the return blade. This point would hinder the rotation of the blade.

Pressure and velocity diagrams for other rotational positions are shown in Figures 20 and 21. In conclusion, during the return process, the addition of the best WEGS has both advantages and disadvantages, with a performance approximately equal to that of the open turbine, but during the advance process, the addition of the best WEGS has a momentous influence on improving the wind-trapping capacity, neutralizing the deficiencies during the return process and maintaining a higher instantaneous torque coefficient throughout the cycle than the open turbine.

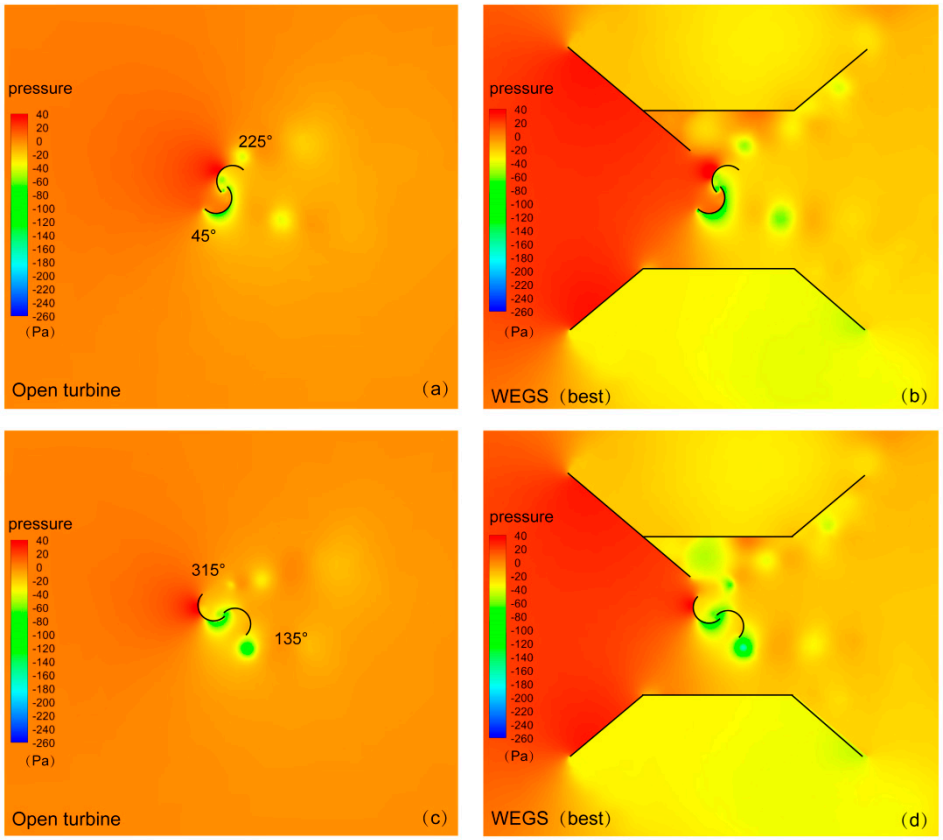


Figure 20. Pressure distribution of an open turbine and a turbine with the best WEGS at other rotational positions (TSR = 1).

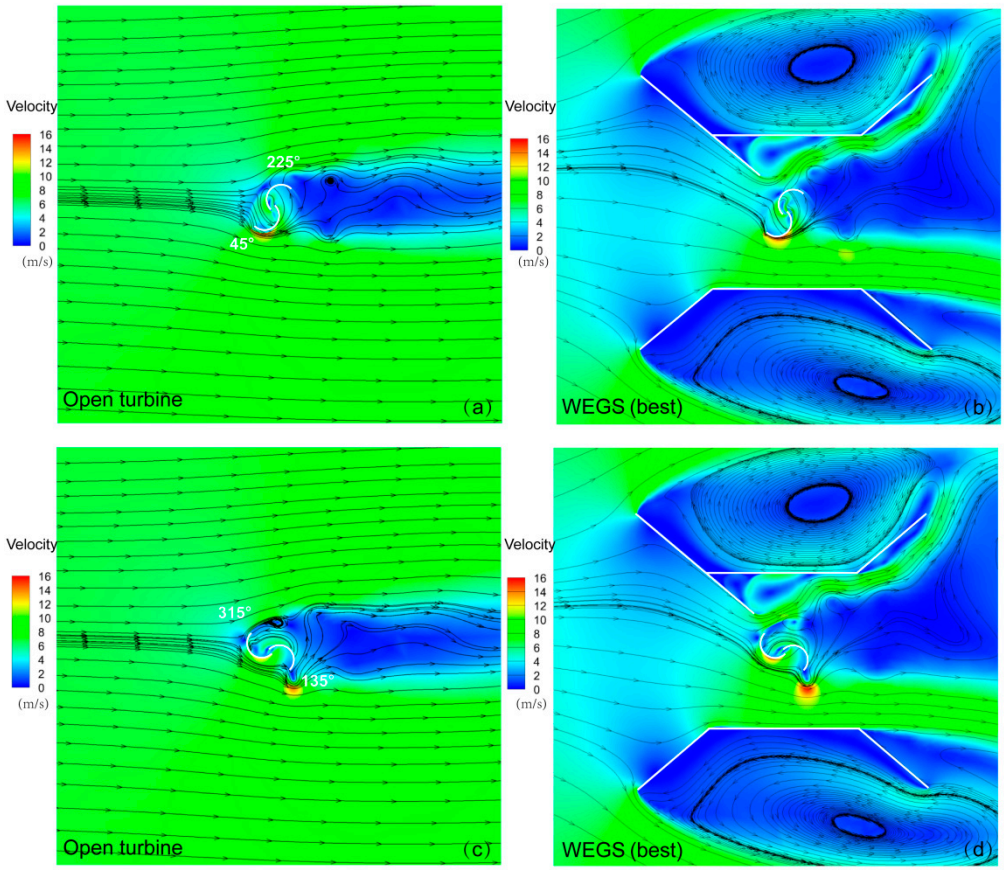


Figure 21. Velocity distribution of an open turbine and a turbine with the best WEGS at other rotational positions (*TSR* = 1).

6. Conclusions

In this work, a new auxiliary structure called the WEGS is proposed to enhance the wind-trapping capacity of a turbine, with the ultimate goal of instantaneously increasing the power at all rotation positions throughout the entire rotation cycle. Several key parameters of the WEGS are optimized with the help of CFD numerical simulation and Taguchi's analytical method, and the performance enhancement mechanism is analyzed based on the flow field distribution. The key conclusions are as follows:

1. CFD simulation results demonstrate that the mean C_t value of the turbine with the best WEGS is 42.1% higher than that of the open turbine at *TSR* = 1 and a wind speed of 7 m/s.
2. At wind speed = 7 m/s, the best WEGS turbines outperform the open turbines by 20.1–53% under other *TSR* conditions. In addition, the best WEGS wind turbine also outperforms the open turbine at other wind speeds.
3. Analysis of variance (ANOVA) results demonstrate that the shrinkage and diffusion angle, the length of the centerboard, and the length of the shrinkage and diffusion tubes are the main structure parameters that would significantly affect the ability of the WEGS to enhance the wind-trapping capacity of the Savonius turbine.
4. While improving the wind turbine's ability to capture wind, the WEGS can also reduce the torque fluctuations of the blade, thereby extending the service life of the turbine.

In the future, more advanced methods such as the combination of agent models and intelligent optimization algorithms, Monte Carlo methods, and machine learning can be used to further optimize the main parameters of the WEGS [50–52].

Author Contributions: Conceptualization, T.Z.; methodology, S.X.; software, T.Z.; validation, T.Z.; formal analysis, T.Z.; investigation, S.X.; resources, S.X.; data curation, T.Z.; writing—original draft preparation, T.Z.; writing—review and editing, T.Z. and S.X.; visualization, S.X.; supervision, S.X.; project administration, S.X.; funding acquisition, S.X. All authors have read and agreed to the published version of the manuscript.

Funding: This research was funded by the National Natural Science Foundation of China (project No. 52375252, 51905284) and the Science, Education and Industry Integration Project of Qilu University of Technology (Grant No. 2023PY019).

Data Availability Statement: The raw data supporting the conclusions of this article will be made available by the authors on request.

Conflicts of Interest: The authors declare no conflicts of interest.

References

1. Ji, X.; Lu, X.; Li, H.; Ma, P.; Xu, S. Blade optimization design of Savonius hydraulic turbine based on radial basis function surrogate model and L-SHADE algorithm. *Ocean Eng.* **2023**, *286*, 115620. [CrossRef]
2. Fatahian, H.; Mishra, R.; Jackson, F.F.; Fatahian, E. Design optimization of an innovative deflector with bleed jets to enhance the performance of dual Savonius turbines using CFD-Taguchi method. *Energy Convers. Manag.* **2023**, *296*, 117655. [CrossRef]
3. Ullah, T.; Javed, A.; Abdullah, A.; Ali, M.; Uddin, E. Computational evaluation of an optimum leading-edge slat deflection angle for dynamic stall control in a novel urban-scale vertical axis wind turbine for low wind speed operation. *Sustain. Energy Technol. Assess.* **2020**, *40*, 100748. [CrossRef]
4. Liu, S.; Zhang, L.; Lu, J.; Zhang, X.; Wang, K.; Gan, Z.; Liu, X.; Jing, Z.; Cui, X.; Wang, H. Advances in urban wind resource development and wind energy harvesters. *Renew. Sustain. Energy Rev.* **2025**, *207*, 114943. [CrossRef]
5. Abdelghafar, I.; Refaie, A.G.; Kerikous, E.; Thévenin, D.; Hoerner, S. Optimum geometry of seashell-shaped wind turbine rotor: Maximizing output power and minimizing thrust. *Energy Convers. Manag.* **2023**, *292*, 117331. [CrossRef]
6. Das Karmakar, S.; Chattopadhyay, H. A review of augmentation methods to enhance the performance of vertical axis wind turbine. *Sustain. Energy Technol. Assess.* **2022**, *53*, 102469. [CrossRef]
7. Belmili, H.; Cheikh, R.; Smail, T.; Seddaoui, N.; Biara, R.W. Study, design and manufacturing of hybrid vertical axis Savonius wind turbine for urban architecture. *Energy Procedia* **2017**, *136*, 330–335. [CrossRef]
8. Elsakka, M.M.; Ingham, D.B.; Ma, L.; Pourkashanian, M. CFD analysis of the angle of attack for a vertical axis wind turbine blade. *Energy Convers. Manag.* **2019**, *182*, 154–165. [CrossRef]
9. Ang, T.-Z.; Salem, M.; Kamarol, M.; Das, H.S.; Nazari, M.A.; Prabaharan, N. A comprehensive study of renewable energy sources: Classifications, challenges and suggestions. *Energy Strategy Rev.* **2022**, *43*, 100939. [CrossRef]
10. Tahani, M.; Rabbani, A.; Kasaeian, A.; Mehrpooya, M.; Mirhosseini, M. Design and numerical investigation of Savonius wind turbine with discharge flow directing capability. *Energy* **2017**, *130*, 327–338. [CrossRef]
11. Nasef, M.H.; El-Askary, W.A.; AbdEl-hamid, A.A.; Gad, H.E. Evaluation of Savonius rotor performance: Static and dynamic studies. *J. Wind Eng. Ind. Aerodyn.* **2013**, *123*, 1–11. [CrossRef]
12. Saha, U.K.; Thotla, S.; Maity, D. Optimum design configuration of Savonius rotor through wind tunnel experiments. *J. Wind Eng. Ind. Aerodyn.* **2008**, *96*, 1359–1375. [CrossRef]
13. Zhao, Z.; Zheng, Y.; Xu, X.; Liu, W.; Hu, G. Research on the improvement of the performance of savonius rotor based on numerical study. In Proceedings of the 2009 International Conference on Sustainable Power Generation and Supply, Nanjing, China, 6–7 April 2009; pp. 1–6.
14. Thiyagaraj, J.; Rahamathullah, I.; Anbuchezhiyan, G.; Barathiraja, R.; Ponshanmugakumar, A. Influence of blade numbers, overlap ratio and modified blades on performance characteristics of the savonius hydro-kinetic turbine. *Mater. Today Proc.* **2021**, *46*, 4047–4053. [CrossRef]
15. Sharma, S.; Sharma, R.K. Performance improvement of Savonius rotor using multiple quarter blades—A CFD investigation. *Energy Convers. Manag.* **2016**, *127*, 43–54. [CrossRef]
16. Sharma, S.; Sharma, R.K. CFD investigation to quantify the effect of layered multiple miniature blades on the performance of Savonius rotor. *Energy Convers. Manag.* **2017**, *144*, 275–285. [CrossRef]
17. Hassan Saeed, H.A.; Nagib Elmekawy, A.M.; Kassab, S.Z. Numerical study of improving Savonius turbine power coefficient by various blade shapes. *Alex. Eng. J.* **2019**, *58*, 429–441. [CrossRef]
18. Abdelghafar, I.; Kerikous, E.; Hoerner, S.; Thévenin, D. Evolutionary optimization of a Savonius rotor with sandeel-inspired blades. *Ocean Eng.* **2023**, *279*, 114504. [CrossRef]
19. Chan, C.M.; Bai, H.L.; He, D.Q. Blade shape optimization of the Savonius wind turbine using a genetic algorithm. *Appl. Energy* **2018**, *213*, 148–157. [CrossRef]
20. Saad, A.S.; El-Sharkawy, I.I.; Ookawara, S.; Ahmed, M. Performance enhancement of twisted-bladed Savonius vertical axis wind turbines. *Energy Convers. Manag.* **2020**, *209*, 112673. [CrossRef]

21. Eshagh Nimvari, M.; Fatahian, H.; Fatahian, E. Performance improvement of a Savonius vertical axis wind turbine using a porous deflector. *Energy Convers. Manag.* **2020**, *220*, 113062. [CrossRef]
22. Payambarpour, S.A.; Najafi, A.F.; Magagnato, F. Investigation of deflector geometry and turbine aspect ratio effect on 3D modified in-pipe hydro Savonius turbine: Parametric study. *Renew. Energy* **2020**, *148*, 44–59. [CrossRef]
23. Chegini, S.; Asadbeigi, M.; Ghafoorian, F.; Mehrpooya, M. An investigation into the self-starting of darrieus-savonius hybrid wind turbine and performance enhancement through innovative deflectors: A CFD approach. *Ocean Eng.* **2023**, *287*, 115910. [CrossRef]
24. Tomar, S.S.; Dewan, A.; Singh, T.P. Effects of axisymmetric-omnidirectional deflector on aerodynamics of modified Bach Savonius rotor for power enhancement. *Energy Convers. Manag.* **2023**, *297*, 117720. [CrossRef]
25. Hesami, A.; Nikseresht, A.H.; Mohamed, M.H. Feasibility study of twin-rotor Savonius wind turbine incorporated with a wind-lens. *Ocean Eng.* **2022**, *247*, 110654. [CrossRef]
26. Mohamed, M.H.; Alqurashi, F.; Thévenin, D. Performance enhancement of a Savonius turbine under effect of frontal guiding plates. *Energy Rep.* **2021**, *7*, 6069–6076. [CrossRef]
27. Chemengich, S.J.; Kassab, S.Z.; Lotfy, E.R. Effect of the variations of the gap flow guides geometry on the savonius wind turbine performance: 2D and 3D studies. *J. Wind Eng. Ind. Aerodyn.* **2022**, *222*, 104920. [CrossRef]
28. Sheldahl, R.E.; Blackwell, B.F.; Feltz, L.V. Wind tunnel performance data for two- and three-bucket Savonius rotors. *J. Energy* **1978**, *2*, 160–164. [CrossRef]
29. Kerikous, E.; Thévenin, D. Performance Enhancement of a Hydraulic Savonius Turbine by Optimizing Overlap and Gap Ratios. In Proceedings of the Gas Turbine India Conference, Chennai, India, 5–6 December 2019.
30. Hassanzadeh, R.; Mohammadnejad, M. Effects of inward and outward overlap ratios on the two-blade Savonius type of vertical axis wind turbine performance. *Int. J. Green Energy* **2019**, *16*, 1485–1496. [CrossRef]
31. Hesami, A.; Nikseresht, A.H. Towards development and optimization of the Savonius wind turbine incorporated with a wind-lens. *Energy* **2023**, *274*, 127263. [CrossRef]
32. Kerikous, E.; Thévenin, D. Optimal shape and position of a thick deflector plate in front of a hydraulic Savonius turbine. *Energy* **2019**, *189*, 116157. [CrossRef]
33. Hashem, I.; Zhu, B. Metamodeling-based parametric optimization of a bio-inspired Savonius-type hydrokinetic turbine. *Renew. Energy* **2021**, *180*, 560–576. [CrossRef]
34. Tian, W.; Song, B.; VanZwieten, J.H.; Pyakurel, P. Computational Fluid Dynamics Prediction of a Modified Savonius Wind Turbine with Novel Blade Shapes. *Energies* **2015**, *8*, 7915–7929. [CrossRef]
35. Tian, W.; Mao, Z.; Zhang, B.; Li, Y. Shape optimization of a Savonius wind rotor with different convex and concave sides. *Renew. Energy* **2018**, *117*, 287–299. [CrossRef]
36. Xia, H.; Zhang, S.; Jia, R.; Qiu, H.; Xu, S. Blade shape optimization of Savonius wind turbine using radial based function model and marine predator algorithm. *Energy Rep.* **2022**, *8*, 12366–12378. [CrossRef]
37. Asadi, M.; Hassanzadeh, R. Effects of internal rotor parameters on the performance of a two bladed Darrieus-two bladed Savonius hybrid wind turbine. *Energy Convers. Manag.* **2021**, *238*, 114109. [CrossRef]
38. Alom, N.; Saha, U.K. Influence of blade profiles on Savonius rotor performance: Numerical simulation and experimental validation. *Energy Convers. Manag.* **2019**, *186*, 267–277. [CrossRef]
39. Gray, C.T. Introduction to quality engineering: Designing quality into products and processes, G. Taguchi, Asian productivity organization, 1986. number of pages: 191. price: $29 (U.K.). *Qual. Reliab. Eng. Int.* **1988**, *4*, 198. [CrossRef]
40. Chen, W.-H.; Wang, J.-S.; Chang, M.-H.; Mutuku, J.K.; Hoang, A.T. Efficiency improvement of a vertical-axis wind turbine using a deflector optimized by Taguchi approach with modified additive method. *Energy Convers. Manag.* **2021**, *245*, 114609. [CrossRef]
41. Khanjanpour, M.H.; Javadi, A.A. Optimization of the hydrodynamic performance of a vertical Axis tidal (VAT) turbine using CFD-Taguchi approach. *Energy Convers. Manag.* **2020**, *222*, 113235. [CrossRef]
42. Qasemi, K.; Azadani, L.N. Optimization of the power output of a vertical axis wind turbine augmented with a flat plate deflector. *Energy* **2020**, *202*, 117745. [CrossRef]
43. Yang, W.H.; Tarng, Y.S. Design optimization of cutting parameters for turning operations based on the Taguchi method. *J. Mater. Process. Technol.* **1998**, *84*, 122–129. [CrossRef]
44. Bademlioglu, A.H.; Canbolat, A.S.; Yamankaradeniz, N.; Kaynakli, O. Investigation of parameters affecting Organic Rankine Cycle efficiency by using Taguchi and ANOVA methods. *Appl. Therm. Eng.* **2018**, *145*, 221–228. [CrossRef]
45. Meyners, M.; Hasted, A. On the applicability of ANOVA models for CATA data. *Food Qual. Prefer.* **2021**, *92*, 104219. [CrossRef]
46. Wang, M.; Rasch, D.; Verdooren, R. Determination of the size of a balanced experiment in mixed ANOVA models using the modified approximate F-test. *J. Stat. Plan. Inference* **2005**, *132*, 183–201. [CrossRef]
47. Simpson, J.R. Taguchi Techniques for Quality Engineering. *J. Qual. Technol.* **1996**, *28*, 487–489. [CrossRef]
48. Liu, Y.-J.; Zeng, T.-W. Evaluation of the effects of synthesis conditions on the crystallite size of SnO_2 nanoparticles via the Taguchi method. *Inorg. Chem. Commun.* **2023**, *156*, 111257. [CrossRef]
49. Zanforlin, S.; Buzzi, F.; Francesconi, M. Performance Analysis of Hydrofoil Shaped and Bi-Directional Diffusers for Cross Flow Tidal Turbines in Single and Double-Rotor Configurations. *Energies* **2019**, *12*, 272. [CrossRef]
50. Giannelos, S.; Bellizio, F.; Strbac, G.; Zhang, T. Machine learning approaches for predictions of CO_2 emissions in the building sector. *Electr. Power Syst. Res.* **2024**, *235*, 110735. [CrossRef]

51. Liao, Z.; Wang, Y.; Xu, J. Based on Big Data: The Analysis of Asian Options Compared With European Options in Chinese Market. In Proceedings of the 2021 2nd International Conference on Big Data Economy and Information Management (BDEIM), Sanya, China, 3–5 December 2021; pp. 76–80.
52. Mitridati, L.; Pinson, P. A Bayesian Inference Approach to Unveil Supply Curves in Electricity Markets. *IEEE Trans. Power Syst.* **2018**, *33*, 2610–2620. [CrossRef]

Disclaimer/Publisher's Note: The statements, opinions and data contained in all publications are solely those of the individual author(s) and contributor(s) and not of MDPI and/or the editor(s). MDPI and/or the editor(s) disclaim responsibility for any injury to people or property resulting from any ideas, methods, instructions or products referred to in the content.